Data report: magnetic properties of sediments and basalts from the Costa Rica subduction margin (Expeditions 334 and 344)[1]

Katerina E. Petronotis,[2] Gary D. Acton,[3] Luigi Jovane,[4] Yong-Xiang Li,[5] and Xixi Zhao[6, 7]

Chapter contents

Abstract

We measured the rock magnetic properties of 24 basalt, sediment, and tephra samples from Costa Rica Sites U1380, U1381, U1413, and U1414. Day plots indicate that most samples are dominated by populations of pseudosingle-domain (PSD) magnetic minerals, with significant contributions of single-domain (SD) grains in the tephra samples and multidomain (MD) grains in the basalts and coarser grained sediments. Coercivity distributions from first-order reversal curves (FORCs) from basalt samples generally peak at about 2–5 mT, rarely extend beyond 20 mT, and show interactions consistent with the presence of PSD and lesser amounts of MD particles. Distributions are consistent with titanomagnetite and/or titanomaghemite being the primary magnetic minerals, as is typical for oceanic basalts. FORCs for the tephras have broad coercivity distributions with peaks near 40–70 mT and with much less interaction than the basalts. The narrow interaction width reflects lower magnetic concentrations than the basalts, whereas the higher coercivity is consistent with the presence of significant SD magnetite, with possibly small amounts of iron sulfides. Coercivity distributions for sediments are typical of marine sediments with mixtures of mainly PSD and SD particles. These distributions have peaks between about 10 and 50 mT, with interactions that are dependent on magnetic concentrations. Demagnetization experiments of basalt samples show that, after the removal of a low-coercivity drilling overprint, the basalts have a primary magnetization component with relatively shallow inclination (~20°), consistent with the tectonic history of the Cocos plate. Basalt samples from the top and flank of the Cocos Ridge have slightly different rock magnetic properties, possibly indicating varying components of hotspot volcanism and seafloor spreading.

Introduction

Magnetic properties of sediments and rocks can be used to identify magnetic carriers and evaluate the fidelity of the paleomagnetic record. This information can be used to determine whether the rocks and sediments have been deformed or chemically altered and whether they are appropriate for determining the magnetostratigraphy of a site.

This pilot study presents the rock magnetic properties of representative basalt, sediment, and tephra samples collected from the

Costa Rica subduction margin off Osa Peninsula during Integrated Ocean Drilling Program (IODP) Expeditions 334 and 344 (Expedition 334 Scientists, 2012a; see the "Expedition 344 summary" chapter [Harris et al., 2013a]). Measurements include magnetic susceptibility, hysteresis, and first-order reversal curves (FORCs). In addition, the natural remanent magnetization (NRM) of a few basalt samples was also measured to investigate the demagnetization behavior, which provides further insights into the rock magnetic properties of the samples as well as information about the reliability of the paleomagnetic signal for tectonic studies that are being conducted on the Expedition 334 and 344 cores.

A goal of both expeditions, which are part of the Costa Rica Seismogenesis Project (CRISP), was to understand the processes that control fault nucleation and seismic rupture for large earthquakes that occur along this convergent margin (Expedition 334 Scientists, 2012a; see the "Expedition 344 summary" chapter [Harris et al., 2013a]). This requires characterization of the lithology, including chemical, physical, and magnetic properties, and the stress, hydrologic, and thermal state of the upper plate. Rock magnetic studies provide part of the characterization by constraining compositional components and yielding information about alteration and magnetic remanence history. The latter is important for chronostratigraphic analysis (e.g., magnetostratigraphy) and for assessing past deformation, such as tilting and vertical-axis rotations.

We analyzed samples that come from both sides of the subduction zone, with sites on the subducting Cocos plate and the overriding Caribbean plate (Fig. F1). Sites U1381 and U1414 are located on the Cocos plate, over crust formed at the Cocos-Nazca spreading center (Barckhausen et al., 2001), and serve as reference sites for the material entering the subduction zone. Site U1381 is located at 2065 m below seafloor (mbsf) on the top of the Cocos Ridge, which was created when Galapagos magmatism intruded the Cocos plate (Walther, 2003). Site U1414 is located at 2459 mbsf on the northern flank of the Cocos Ridge, in what could be described as Cocos plate transitional crust. Sites U1380 (503 mbsf) and U1413 (540 mbsf) are located on the middle and upper slope of the Caribbean plate, respectively, and record the subsidence and erosion history of the margin (Ranero and Von Huene, 2000; Vannucchi et al., 2001).

Methods

Magnetic hysteresis

Magnetic hysteresis properties of samples were measured with an alternating gradient magnetometer (Princeton Measurements Corporation MicroMag 2900) at the Paleomagnetism Laboratory of the University of California at Davis (UC Davis; USA). We selected a range of lithologies that correspond to the major lithostratigraphic units identified during the expedition (Expedition 334 Scientists, 2012b; see the "Input Site U1381," "Input Site U1414," "Midslope Site U1380," and "Upper slope Site U1413" chapters [Harris et al., 2013b, 2013c, 2013e, 2013f]). All hysteresis measurements presented in this study were made on basalt chips or sediment specimens taken from the working halves of core sections (see the "Methods" chapter [Harris et al., 2013d] for curatorial procedures used on board the *JOIDES Resolution*).

Magnetic hysteresis properties are presented using Day plots (Day et al., 1977) and FORC diagrams (Pike et al., 1999; Roberts et al., 2000). Day plots display the ratio of saturation remanent magnetization to saturation magnetization (M_{rs}/M_s) versus the ratio of coercivity of remanence to coercive force (H_{cr}/H_c) and can be used to characterize the bulk magnetic assemblage of particles as being single-domain (SD), pseudosingle-domain (PSD), or multidomain (MD), as defined by Dunlop (2002). However, the combination of different mineral compositions and grain sizes and the interactions among magnetic grains can lead to results that are difficult to interpret.

FORC diagrams can be used to discriminate the coercivities of magnetic grains and their interactions. A FORC diagram is a contour plot of H_a versus H_c, where H_a represents the applied magnetic field interacting with the sample and H_c represents the coercivity of the magnetic particles in the sample (Pike et al., 1999). The shapes of the coercivity and interaction distributions are indicative of magnetic properties and can aid in determining the types of magnetic minerals present in the samples. For example, a population of noninteracting SD grains with a single coercivity (H1) would be represented by contours with small vertical and horizontal range around $H_a = 0$, $H_c = H1$. Contours that are elongated narrowly along the $H_a = 0$ axis indicate the presence of populations of noninteracting SD grains with varying coer-

civities, whereas contours with a larger vertical span indicate interactions between particles or within particles, such as within PSD or MD grains. Interactions between multiple populations of SD, PSD, and/or MD grains can produce much larger vertical spread and sometimes lobes and valleys on the FORC diagrams. For the diagrams presented here, we used a minimum of 120 curves to construct each FORC diagram.

Natural remanent magnetization

The NRMs of a few basalt samples were measured to investigate their demagnetization behavior. Cubes with volumes of 1.0–1.9 cm³ and masses of 2.6–5.3 g were cut out of the working halves of core sections and come from the same intervals as the basalt chips used for the hysteresis measurements. The cube samples were step-wise, progressively demagnetized in an alternating field (AF) up to peak fields of 60 mT, with one sample demagnetized up to 100 mT. The magnetization direction and intensity was measured after each demagnetization step with a 2G Enterprises 755R cryogenic magnetometer. The magnetic susceptibility of the cubes was measured before the samples were demagnetized.

Results

Magnetic hysteresis of basalt samples

Table **T1** presents hysteresis data for basalts recovered from Expedition 344 Hole U1414A (see the **"Input Site U1414"** chapter [Harris et al., 2013c]) and Expedition 334 Hole U1381A (Expedition 334 Scientists, 2012b). Figure **F2** presents the basalt data on a Day plot relative to the SD, PSD, and MD fields defined by Dunlop (2002). The gray curves on this plot represent the theoretical SD versus MD mixing lines of Dunlop (2002), which are based on ideal mixtures of different magnetite grain sizes. The two groups of basalt samples differ slightly in their magnetic hysteresis properties. Both groups fall in the PSD field, but pillow lava samples from the top of the Cocos Ridge (Hole U1381A; light blue symbols) show an even distribution of SD and MD grains, whereas massive lava flow samples from the flank of the Cocos Ridge (Hole U1414A; dark blue symbols) indicate a higher contribution of MD grains.

The FORC diagrams generated for Hole U1414A and U1381A basalt samples are displayed in Figure **F3.** All diagrams have relatively circular contours with peak values of only 2–5 mT, indicating the predominance of a low-coercivity magnetic mineral. Given how common it is in oceanic basalts, this mineral is most likely titanomagnetite or its low-temperature oxi-

dized counterpart titanomaghemite. The vertical spread of the contours suggests the presence of interacting grains of mainly PSD and MD sizes. The sample from Hole U1381A (top of Cocos Ridge) has lower magnetic interactions, a smaller contribution from MD grains, and a higher coercivity component than the Hole U1414 samples (Cocos Ridge flank), the latter of which could originate from finer grained PSD and/or SD particles (Fig. **F3**).

Magnetic hysteresis of tephra samples

Table **T2** presents hysteresis data from one of the tephra layers recovered from Expedition 344 Hole U1381C (see the **"Input Site U1381"** chapter [Harris et al., 2013b]). For these measurements, we collected a vertical transect of samples from the top to the bottom of a thick, graded tephra layer recovered in Section 344-U1381C-7H-2. Figure **F2** presents the tephra data on a Day plot relative to the SD, PSD, and MD fields defined by Dunlop (2002). Figure **F4** displays the same data (Samples 2–8) on a magnified portion of the Day plot. Nannofossil ooze data from the same core section (Samples 1 and 9) are also shown to compare the properties of the tephra layer with those of the background carbonate lithology that dominates this cored interval. Samples from the top and middle portions of the tephra layer cluster in the SD field, whereas samples from the bottom portion of the tephra layer and the nannofossil ooze background lithology fall in the PSD field (Fig. **F4**). This is consistent with the normally graded nature of this tephra layer (see the **"Input Site U1381"** chapter [Harris et al., 2013b]).

The FORC diagrams generated for two of the tephra samples display similar patterns (Fig. **F5**). The closed, elongated contours and small vertical spread suggest assemblages dominated by noninteracting SD grains. The range of coercivity values indicates the predominance of magnetite with a possible contribution from iron sulfides (e.g., pyrrhotite). A secondary peak present near the *y*-axis suggests a small contribution of grains with very low coercivity, which may be a processing artifact or could indicate a small contribution from larger grains (MD and PSD).

Magnetic hysteresis of sediment samples

Table **T3** presents hysteresis data for sediments recovered from Expedition 344 Holes U1381C, U1414A, U1380C, and U1413A (see the **"Input Site U1381," "Input Site U1414," "Mid-slope Site U1380,"** and **"Upper slope Site U1413"** chapters [Harris et al., 2013b, 2013c, 2013e, 2013f]). This group of samples comprises a variety of fine- to coarse-grained lithologies that are representative of the sediments recovered from the Costa Rica conver-

gent margin. A sample from a recrystallized, calcareous sandstone encountered between lava flows in Hole U1414A is also included in this group (see the "Input Site U1414" chapter [Harris et al., 2013c]). Figure F2 presents the sediment data on a Day plot relative to the SD, PSD, and MD fields defined by Dunlop (2002). The fine-, medium-, and coarse-grained lithologies recovered from the Costa Rica sites all fall in the PSD spectrum (Fig. F2). However, there is a clear progression with grain size, with the carbonate ooze samples showing a larger contribution of SD grains, the clay and silt/siltstone samples showing an even distribution of SD and MD grains, and the sand/sandstone samples showing a larger contribution of MD grains. The recrystallized sandstone sample falls between the sediment and basalt groups of samples and shows a smaller contribution of MD grains relative to the unaltered sand/sandstone samples.

The FORC diagrams generated for the sediment samples suggest a variety of magnetic grain assemblages (Fig. F6). The FORC diagram for the nannofossil ooze in Section 334-U1381C-7H-2 indicates the presence of noninteracting SD grains. The FORC diagrams for the clayey silt in Section 334-U1381C-6H-3 and the sandstone in Section 344-U1380C-25R-2 indicate the presence of PSD grains. The range of coercivities suggests that magnetite is the dominant mineral. Small amounts of iron sulfides may also be present, which is consistent with accessory minerals observed in the sediments (see the "Input Site U1381" chapter [Harris et al., 2013b]). Reliable FORC diagrams could not be obtained for the rest of the coarser grained samples.

Natural remanent magnetization of basalt samples

We measured the magnetization of three samples from Hole U1381A and six basalt samples from Hole U1414A. Changes in NRM during demagnetization are displayed using orthogonal vector endpoint projections (Zijderveld, 1967; Figs. F7, F8). The intensity plots show that AF demagnetization was sufficient to completely demagnetize the samples (Figs. F7, F8). Magnetic directions were determined using principal component analysis (PCA; Kirschvink, 1980). For the PCA analyses, we used 5 points to determine the best-fit lines and anchored the lines to the origin.

The magnetic directions we calculated for the nine basalt samples are provided in Table T4. Because these samples come from unoriented rotary cores, only the inclination values are useful. PCA directions are generally considered reliable if the maximum angular deviation (MAD) of the PCA analysis is relatively small (<10°). Only one of the nine samples ex-

ceeds this limit; all the others are <7°. The one outlier gives the steepest inclination (45.5°). The inclination values for the other eight samples range from –27.3° to 30.4°. The average inclinations of the Hole U1381A and Hole U1414A samples are 20.2° and 18.1°, respectively. These inclination values are consistent with a Cocos plate paleolatitude within ~10° of the Equator around 14 Ma, the age of the crust offshore Osa Peninsula (Barckhausen et al., 2001). However, because these samples do not come from a sufficient number of cooling units to average secular variation, we intend to combine these results with larger postcruise studies.

Interestingly, the two groups of samples are characterized by different magnetic susceptibilities, with a Hole U1381A (top of Cocos Ridge) average of 121 cm³/g and a Hole U1414A (Cocos Ridge flank) average of 287 cm³/g (Table T4).

Conclusion

The magnetic assemblages of Cocos Ridge basalts from Sites U1381 and U1414 are dominated by populations of PSD grains, with varying contributions from MD grains. The basalt samples collected from the top and the flank of the Cocos Ridge are characterized by slightly different rock magnetic properties, perhaps as a result of varying components of hotspot volcanism and seafloor spreading.

Demagnetization experiments of basalt samples show that AF demagnetization is sufficient to isolate a primary remanent magnetization component. The inclination values obtained from the basalts are consistent with the near-equatorial paleolatitude of the Cocos plate when the crust was formed. These results will be combined with larger tectonic studies that are in progress.

Tephra samples from Site U1381 are dominated by SD and PSD grains with much higher coercivities than the basalts and lower magnetic–grain interactions. Grain size depends on stratigraphic depth within thick tephra layers, with PSD grain sizes occurring near the base of a tephra layer and SD grain sizes near the top, consistent with the tephras being normally graded beds. The relatively high coercivities (40–70 mT) and small grain sizes are indicative of SD magnetite, with possible contributions from iron sulfides.

The magnetic assemblages of sediments from Sites U1380, U1381, U1413, and U1414 are dominated by populations of PSD grains, with smaller contributions from SD and MD grains. Sediment coercivities are generally higher than the basalts and lower than the tephras, and the range indicates that magnetite is the dominant mineral.

Acknowledgments

References

Barckhausen, U., Ranero, C.R., von Huene, R., Cande, S.C., and Roeser, H.A., 2001. Revised tectonic boundaries in the Cocos plate off Costa Rica: implications for the segmentation of the convergent margin and for plate tectonic models. *Journal of Geophysical Research: Solid Earth,* 106(B9):19207–19220. http://dx.doi.org/10.1029/2001JB000238

Day, R., Fuller, M., and Schmidt, V.A., 1977. Hysteresis properties of titanomagnetites: grain-size and compositional dependence. *Physics of the Earth and Planetary Interiors,* 13(4):260–267. http://dx.doi.org/10.1016/0031-9201(77)90108-X

Dunlop, D.J., 2002. Theory and application of the Day plot (M_{rs}/M_s versus H_{cr}/H_c), 1. Theoretical curves and tests using titanomagnetite data. *Journal of Geophysical Research: Solid Earth,* 107(B3):2056. http://dx.doi.org/10.1029/2001JB000486

Expedition 334 Scientists, 2012a. Expedition 334 summary. *In* Vannucchi, P., Ujiie, K., Stroncik, N., Malinverno, A., and the Expedition 334 Scientists, *Proceedings of the Integrated Ocean Drilling Program,* 334: Tokyo (Integrated Ocean Drilling Program Management International, Inc.). http://dx.doi.org/10.2204/iodp.proc.334.101.2012

Expedition 334 Scientists, 2012b. Site U1381. *In* Vannucchi, P., Ujiie, K., Stroncik, N., Malinverno, A., and the Expedition 334 Scientists, *Proceedings of the Integrated Ocean Drilling Program,* 334: Tokyo (Integrated Ocean Drilling Program Management International, Inc.). http://dx.doi.org/10.2204/iodp.proc.334.106.2012

Harris, R.N., Sakaguchi, A., Petronotis, K., Baxter, A.T., Berg, R., Burkett, A., Charpentier, D., Choi, J., Diz Ferreiro, P., Hamahashi, M., Hashimoto, Y., Heydolph, K., Jovane, L., Kastner, M., Kurz, W., Kutterolf, S.O., Li, Y., Malinverno, A., Martin, K.M., Millan, C., Nascimento, D.B., Saito, S., Sandoval Gutierrez, M.I., Screaton, E.J., Smith-Duque, C.E., Solomon, E.A., Straub, S.M., Tanikawa, W., Torres, M.E., Uchimura, H., Vannucchi, P., Yamamoto, Y., Yan, Q., and Zhao, X., 2013a. Expedition 344 summary. *In* Harris, R.N., Sakaguchi, A., Petronotis, K., and the Expedition 344 Scientists, *Proceedings of the Integrated Ocean Drilling Program,* 344: College Station, TX (Integrated Ocean Drilling Program). http://dx.doi.org/10.2204/iodp.proc.344.101.2013

Harris, R.N., Sakaguchi, A., Petronotis, K., Baxter, A.T., Berg, R., Burkett, A., Charpentier, D., Choi, J., Diz Ferreiro, P., Hamahashi, M., Hashimoto, Y., Heydolph, K., Jovane, L., Kastner, M., Kurz, W., Kutterolf, S.O., Li, Y., Malinverno, A., Martin, K.M., Millan, C., Nascimento, D.B., Saito, S., Sandoval Gutierrez, M.I., Screaton, E.J., Smith-Duque, C.E., Solomon, E.A., Straub, S.M., Tanikawa, W., Torres, M.E., Uchimura, H., Vannucchi, P., Yamamoto, Y., Yan, Q., and Zhao, X., 2013b. Input Site U1381. *In* Harris, R.N., Sakaguchi, A., Petronotis, K., and the Expedition 344 Scientists, *Proceedings of the Integrated Ocean Drilling Program,* 344: College Station, TX (Integrated Ocean Drilling Program). http://dx.doi.org/10.2204/iodp.proc.344.103.2013

Harris, R.N., Sakaguchi, A., Petronotis, K., Baxter, A.T., Berg, R., Burkett, A., Charpentier, D., Choi, J., Diz Ferreiro, P., Hamahashi, M., Hashimoto, Y., Heydolph, K., Jovane, L., Kastner, M., Kurz, W., Kutterolf, S.O., Li, Y., Malinverno, A., Martin, K.M., Millan, C., Nascimento, D.B., Saito, S., Sandoval Gutierrez, M.I., Screaton, E.J., Smith-Duque, C.E., Solomon, E.A., Straub, S.M., Tanikawa, W., Torres, M.E., Uchimura, H., Vannucchi, P., Yamamoto, Y., Yan, Q., and Zhao, X., 2013c. Input Site U1414. *In* Harris, R.N., Sakaguchi, A., Petronotis, K., and the Expedition 344 Scientists, *Proceedings of the Integrated Ocean Drilling Program,* 344: College Station, TX (Integrated Ocean Drilling Program). http://dx.doi.org/10.2204/iodp.proc.344.104.2013

Harris, R.N., Sakaguchi, A., Petronotis, K., Baxter, A.T., Berg, R., Burkett, A., Charpentier, D., Choi, J., Diz Ferreiro, P., Hamahashi, M., Hashimoto, Y., Heydolph, K., Jovane, L., Kastner, M., Kurz, W., Kutterolf, S.O., Li, Y., Malinverno, A., Martin, K.M., Millan, C., Nascimento, D.B., Saito, S., Sandoval Gutierrez, M.I., Screaton, E.J., Smith-Duque, C.E., Solomon, E.A., Straub, S.M., Tanikawa, W., Torres, M.E., Uchimura, H., Vannucchi, P., Yamamoto, Y., Yan, Q., and Zhao, X., 2013d. Methods. *In* Harris, R.N., Sakaguchi, A., Petronotis, K., and the Expedition 344 Scientists, *Proceedings of the Integrated Ocean Drilling Program,* 344: College Station, TX (Integrated Ocean Drilling Program). http://dx.doi.org/10.2204/iodp.proc.344.102.2013

Harris, R.N., Sakaguchi, A., Petronotis, K., Baxter, A.T., Berg, R., Burkett, A., Charpentier, D., Choi, J., Diz Ferreiro, P., Hamahashi, M., Hashimoto, Y., Heydolph, K., Jovane, L., Kastner, M., Kurz, W., Kutterolf, S.O., Li, Y., Malinverno, A., Martin, K.M., Millan, C., Nascimento, D.B., Saito, S., Sandoval Gutierrez, M.I., Screaton, E.J., Smith-Duque, C.E., Solomon, E.A., Straub, S.M., Tanikawa, W., Torres, M.E., Uchimura, H., Vannucchi, P., Yamamoto, Y., Yan, Q., and Zhao, X., 2013e. Mid-slope Site U1380. *In* Harris, R.N., Sakaguchi, A., Petronotis, K., and the Expedition 344 Scientists, *Proceedings of the Integrated Ocean Drilling Program,* 344: College Station, TX (Integrated Ocean Drilling Program). http://dx.doi.org/10.2204/iodp.proc.344.106.2013

Harris, R.N., Sakaguchi, A., Petronotis, K., Baxter, A.T., Berg, R., Burkett, A., Charpentier, D., Choi, J., Diz Ferreiro, P., Hamahashi, M., Hashimoto, Y., Heydolph, K., Jovane, L., Kastner, M., Kurz, W., Kutterolf, S.O., Li, Y., Malinverno, A., Martin, K.M., Millan, C., Nascimento, D.B., Saito, S., Sandoval Gutierrez, M.I., Screaton, E.J., Smith-Duque, C.E., Solomon, E.A., Straub, S.M., Tanikawa, W., Torres, M.E., Uchimura, H., Vannucchi, P., Yamamoto, Y., Yan, Q., and Zhao, X., 2013f. Upper slope Site U1413. *In* Harris, R.N., Sakaguchi, A., Petronotis, K., and the Expedition 344 Scientists, *Proceedings of the Integrated Ocean Drilling Program,* 344: College Station, TX (Integrated Ocean Drilling Program). http://dx.doi.org/10.2204/iodp.proc.344.107.2013

Kirschvink, J.L., 1980. The least-squares line and plane and the analysis of palaeomagnetic data. *Geophysical Journal of the Royal Astronomical Society,* 62(3):699–718. http://dx.doi.org/10.1111/j.1365-246X.1980.tb02601.x

Pike, C.R., Roberts, A.P., and Verosub, K.L., 1999. Characterizing interactions in fine magnetic particle systems using first order reversal curves. *Journal of Applied Physics*, 85(9):6660–6667. http://dx.doi.org/10.1063/1.370176

Ranero, C.R., and von Huene, R., 2000. Subduction erosion along the Middle America convergent margin. *Nature,* 404(6779):748–752. http://dx.doi.org/10.1038/35008046

Roberts, A.P., Pike, C.R., and Verosub, K.L., 2000. First-order reversal curve diagrams: a new tool for characterizing the magnetic properties of natural samples. *Journal of Geophysical Research: Solid Earth,* 105(B12):28461–28475. http://dx.doi.org/10.1029/2000JB900326

Vannucchi, P., Scholl, D.W., Meschede, M., and McDougall-Reid, K., 2001. Tectonic erosion and consequent collapse of the Pacific margin of Costa Rica: combined implications from ODP Leg 170, seismic offshore data, and regional geology of the Nicoya Peninsula. *Tectonics,* 20(5):649–668. http://dx.doi.org/10.1029/2000TC001223

Walther, C.H.E., 2003. The crustal structure of the Cocos Ridge off Costa Rica. *Journal of Geophysical Research: Solid Earth,* 108(B3):2136. http://dx.doi.org/10.1029/2001JB000888

Zidjerveld, J.D.A., 1967. A.C. demagnetization of rocks: analysis of results. *In* Collinson, D.W., Creer, K.N., and Runcorn, S.K. (Eds.), *Methods in Paleomagnetism:* Amsterdam (Elsevier), 254–286.

Figure F1. Location of Sites U1380, U1381, U1413, and U1414 drilled on the Costa Rica subduction margin during Expeditions 334 and 344.
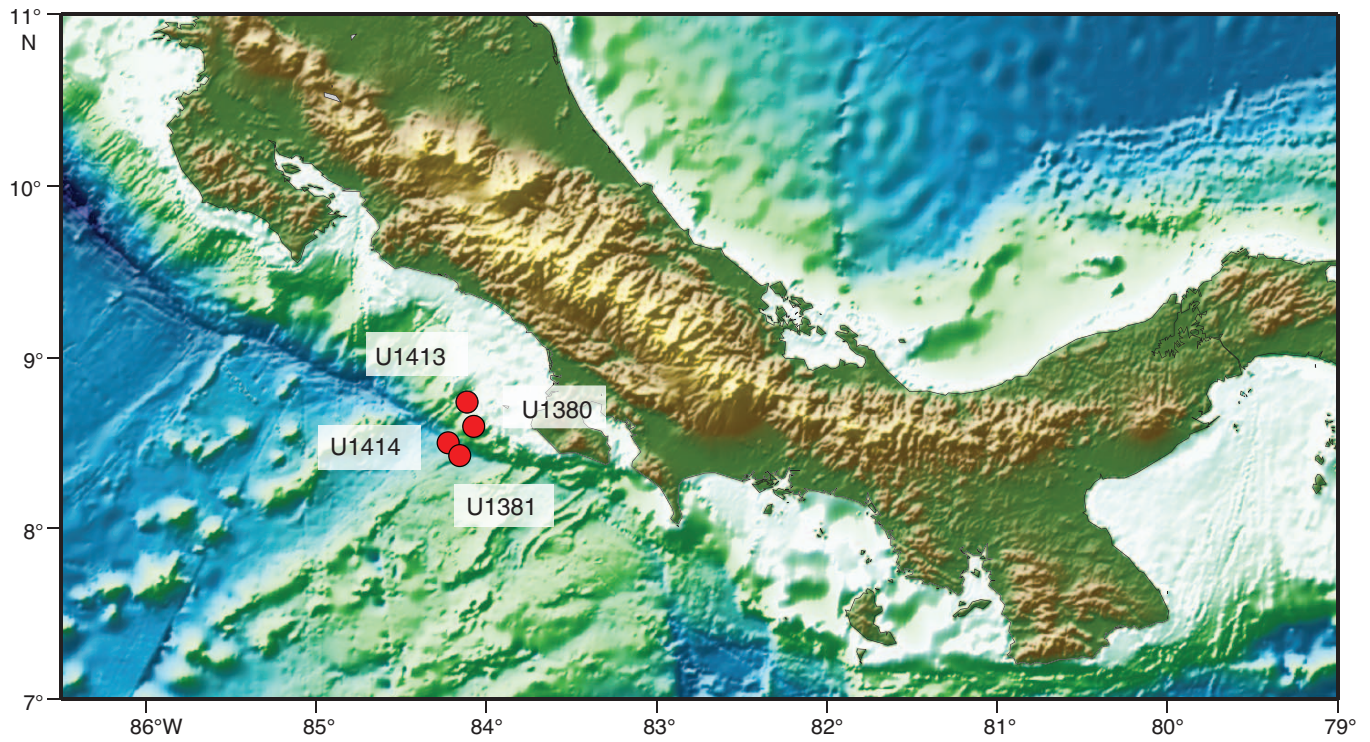
Figure F2. Magnetic hysteresis properties of sediment, tephra, and basalt samples, Sites U1380, U1381, U1413, and U1414.
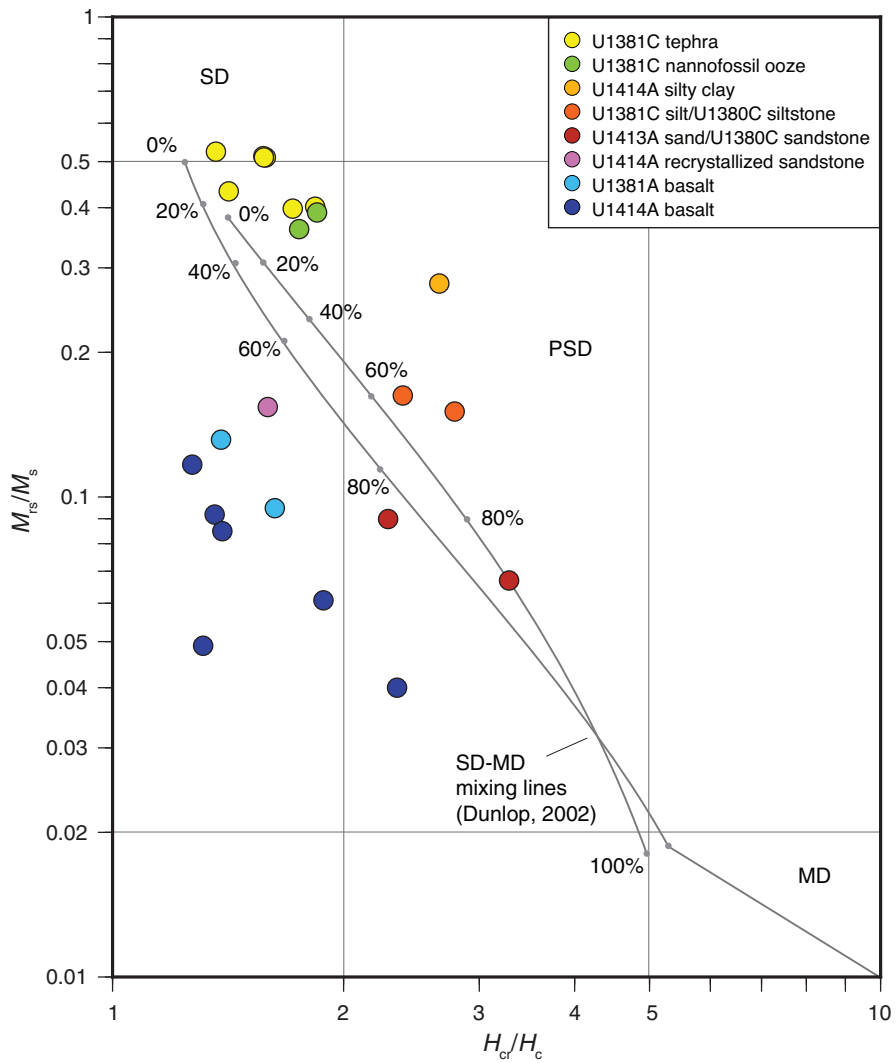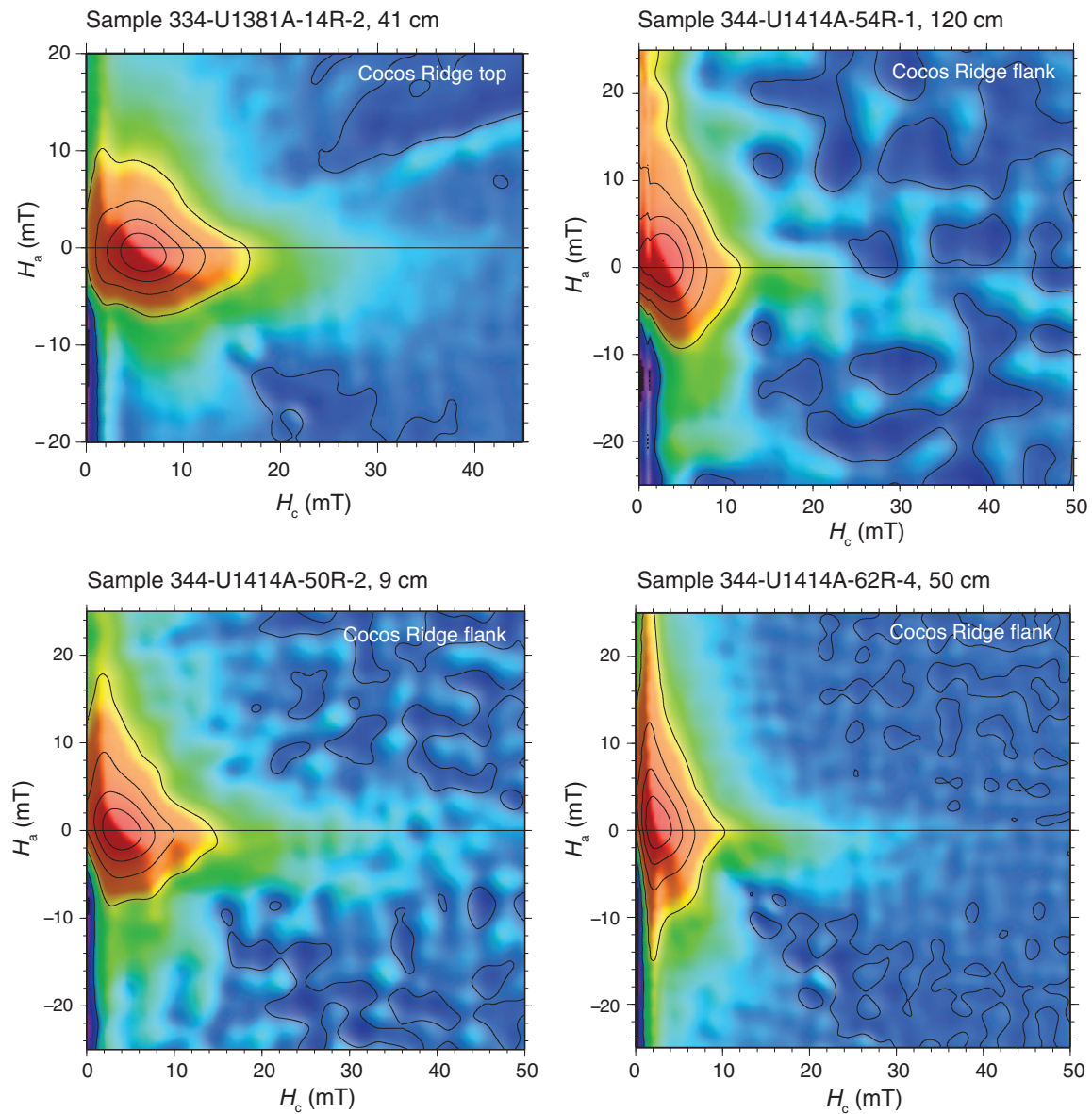
Figure F3. First-order reversal curve (FORC) diagrams of basalts, Sites U1381 and U1414.

Figure F4. Magnetic hysteresis properties of a graded tephra layer, Site U1381. Core image shows the upper part of Section 344-U1381C-7H-2 (57.1–57.9 mbsf) with the tephra layer (dark brown), background nannofossil ooze lithology (light brown), and locations of Samples 1–9.
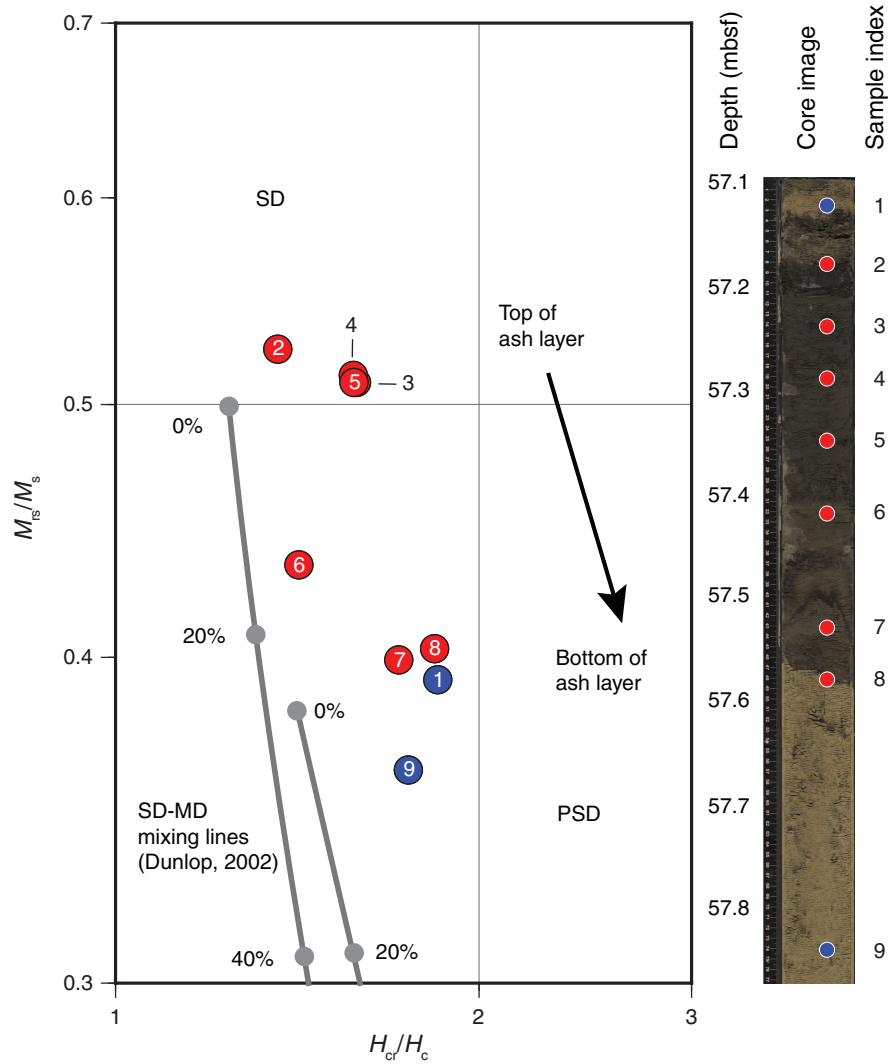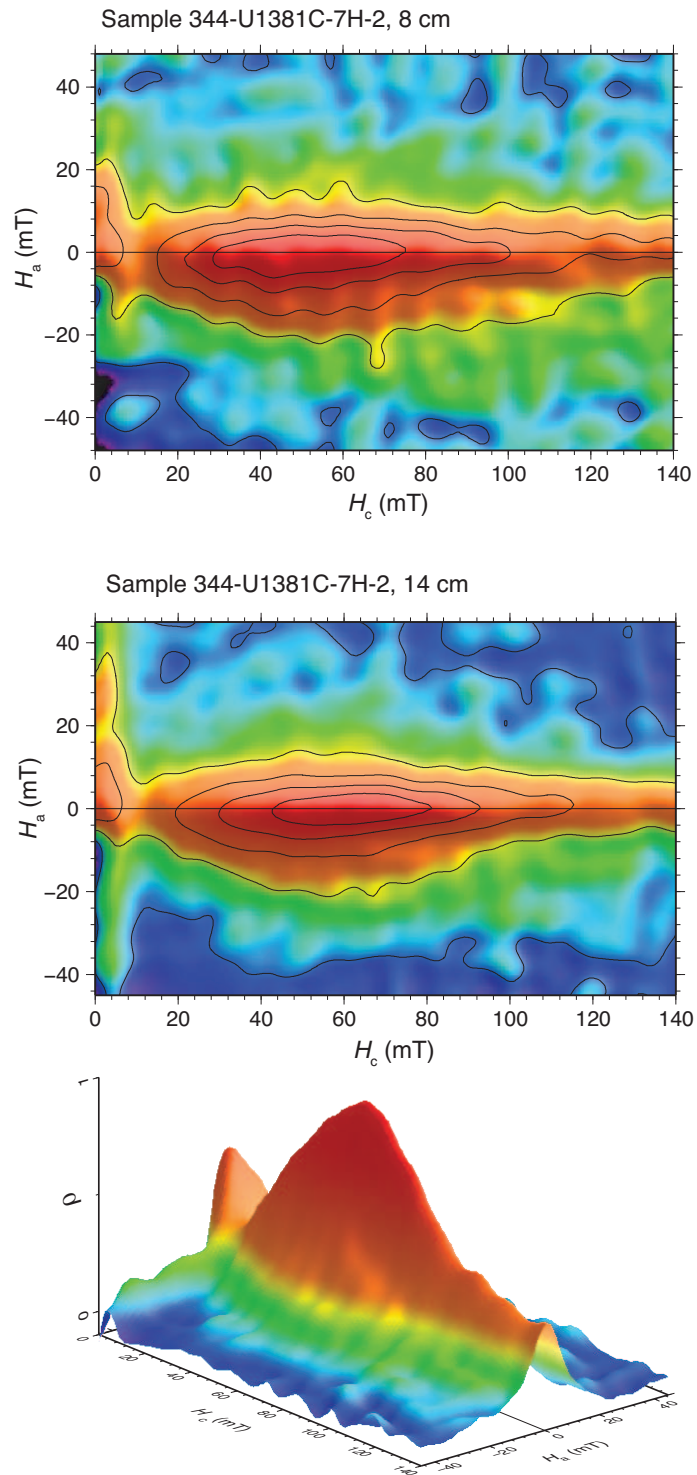
Figure F5. First-order reversal curve (FORC) diagrams of tephra, Site U1381.
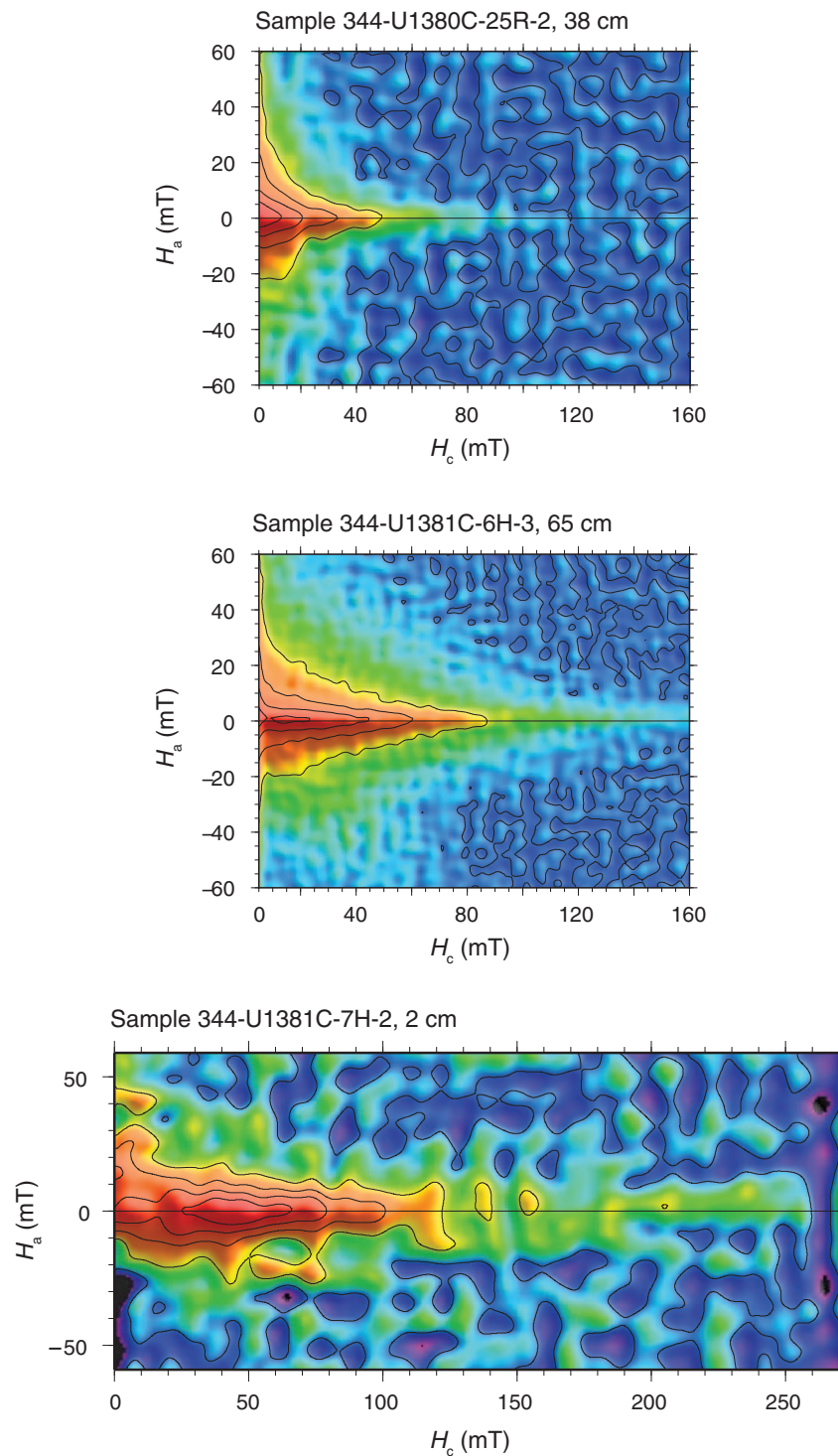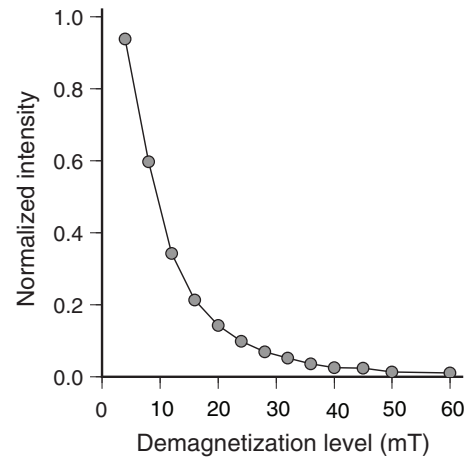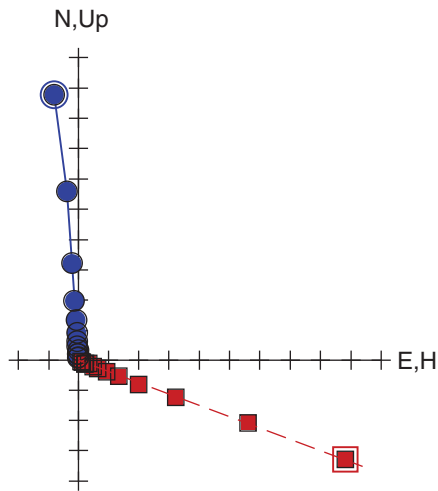
Figure F6. First-order reversal curve (FORC) diagrams of sediments, Sites U1380 and U1381.

Figure F7. Examples of demagnetization experiments, Site U1381. Red squares = inclination data, blue circles = declination data.

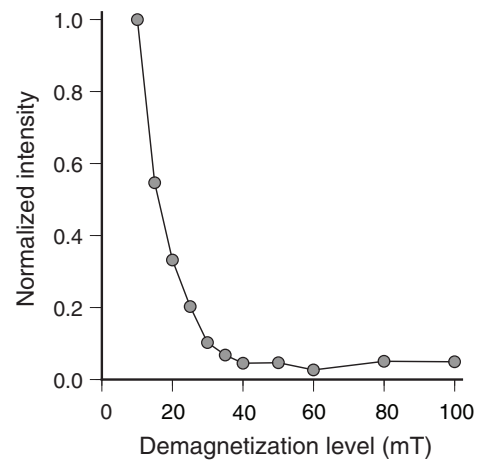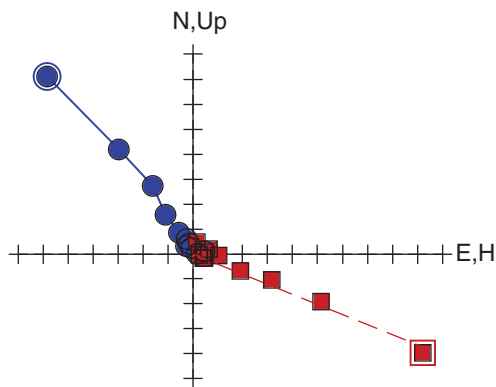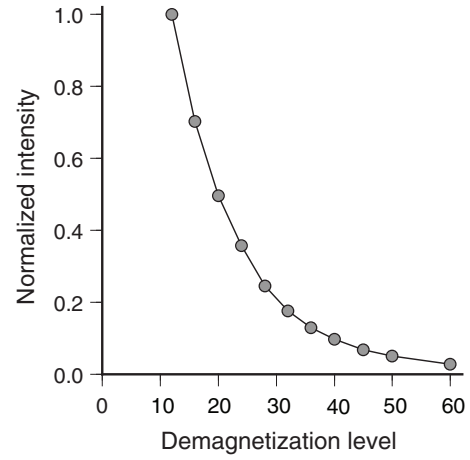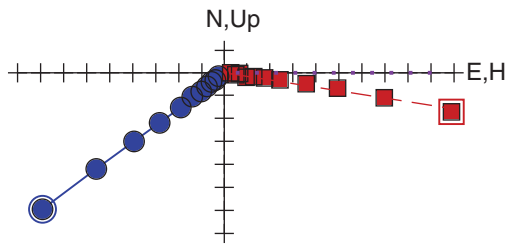Sample 334-U1381A-14R-2, 41 cm

Sample 334-U1381A-24R-1, 52 cm

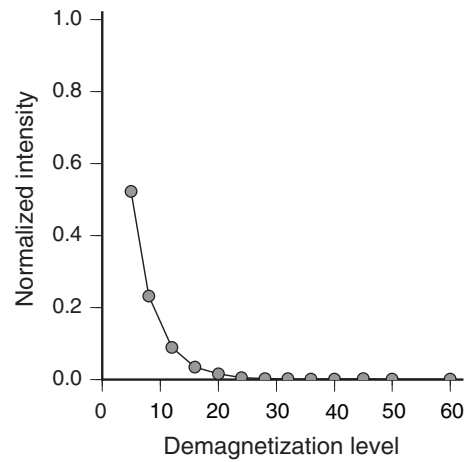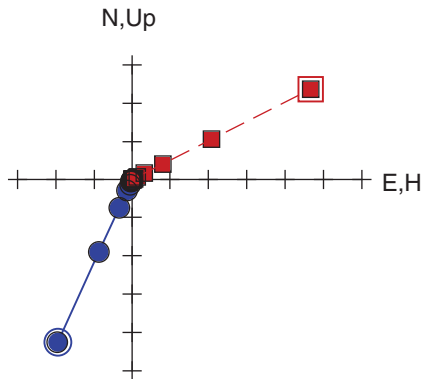**Figure F8.** Examples of demagnetization experiments, Site U1414. Red squares = inclination data, blue circles = declination data.
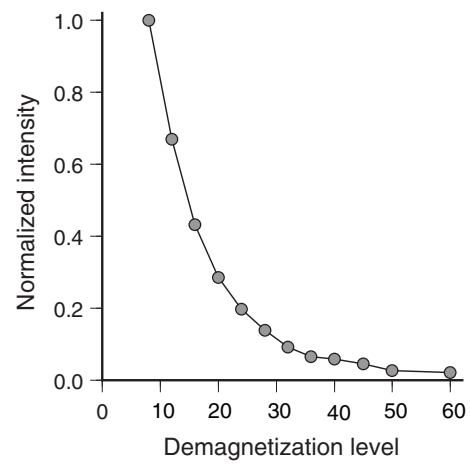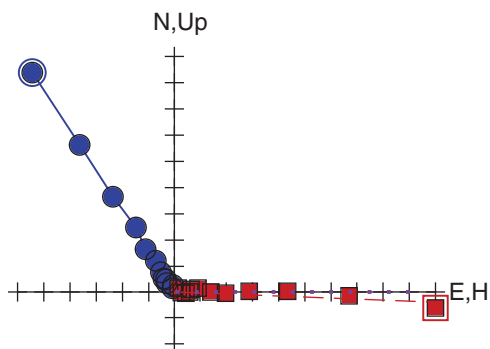
Table T1. Magnetic hysteresis properties of basalts, Sites U1381 and U1414.

Core, section, interval (cm)	Depth (mbsf)	Mass (mg)	M_r (emu)	M_s (emu)	H_{cr} (Oe)	H_c (Oe)	M_r/M_s	H_{cr}/H_c	Igneous unit
334-U1381A-									
14R-2, 41–42	110.39	33	5.100E–03	2.542E–02	66.73	68.23	0.201	0.978	III
19R-1, 65–66	133.05	26	4.201E–03	3.184E–02	71.20	51.37	0.132	1.386	III
24R-1, 52–53*	154.02	32	3.047E–03	3.214E–02	70.57	43.34	0.095	1.628	III
344-U1414A-									
46R-2, 87–88	378.41	46	4.765E–03	4.059E–02	75.05	44.93	0.117	1.270	1
50R-2, 9–10	400.29	42	9.298E–03	1.014E–01	69.57	51.15	0.092	1.360	3
54R-1, 120–121	419.40	53	7.272E–03	1.193E–01	64.49	34.22	0.061	1.885	5
58R-3, 40–41	440.69	24	1.907E–03	4.816E–02	76.51	32.57	0.040	2.349	8
60R-1, 53–54	447.83	35	7.108E–03	8.314E–02	72.21	51.91	0.085	1.391	8
62R-4, 50–51	461.57	34	3.587E–03	7.358E–02	45.18	34.40	0.049	1.313	8

* = not shown on Figure **F2**. Igneous units are from **Harris et al.** (2013c) and Expedition 334 Scientists (2012b).

Table T2. Magnetic hysteresis properties of tephra, Site U1381.

Core, section, interval (cm)	Depth (mbsf)	Mass (mg)	M_r (emu)	M_s (emu)	H_{cr} (Oe)	H_c (Oe)	M_r/M_s	H_{cr}/H_c	Location within tephra layer
344-U1381C-									
7H-2, 8	57.18	15	2.362E–01	4.494E–01	1039.0	762.00	0.525	1.364	Near top contact
7H-2, 14	57.24	25	3.599E–01	7.051E–01	1237.5	781.45	0.510	1.584	Upper interval
7H-2, 19	57.29	23	3.230E–01	6.293E–01	1274.5	809.75	0.513	1.574	Upper interval
7H-2, 25	57.35	19	2.504E–01	4.909E–01	1306.5	829.20	0.510	1.576	Middle interval
7H-2, 32	57.42	14	3.230E–05	7.450E–05	891.75	628.50	0.434	1.419	Middle interval
7H-2, 43	57.53	25	3.130E–05	7.847E–05	942.10	548.70	0.399	1.717	Lower interval
7H-2, 48	57.58	32	5.514E–05	1.368E–04	1050.0	571.25	0.403	1.838	Bottom contact

Table T3. Magnetic hysteresis properties of sediments, Sites U1380, U1381, U1413, and U1414.

Core, section, interval (cm)	Depth (mbsf)	Mass (mg)	M_r (emu)	M_s (emu)	H_{cr} (Oe)	H_c (Oe)	M_r/M_s	H_{cr}/H_c	Lithologic unit	Lithologic description
344-U1380C-										
25R-2, 38	662.46	25	8.917E–05	9.878E–04	164.35	71.94	0.090	2.285	II	Sandstone
44R-1, 74	754.24	29	2.959E–05	1.814E–04	237.95	99.57	0.163	2.390	II	Siltstone
344-U1381C-										
6H-3, 65	49.81	20	5.299E–04	3.511E–03	387.80	139.05	0.151	2.789	I	Clayey silt
7H-2, 2	57.12	15	6.344E–05	1.618E–04	719.45	389.10	0.392	1.849	II	Nannofossil ooze
7H-2, 74	57.84	15	7.223E–06	1.997E–05	577.90	330.15	0.362	1.750	II	Nannofossil ooze
344-U1413A-										
4H-4, 67	30.58	37	7.261E–05	1.079E–03	197.15	59.97	0.067	3.287	I	Sand
344-U1414A-										
3H-4, 59	16.22	39	6.566E–05	2.355E–04	732.10	274.75	0.279	2.665	I	Silty clay
58R-1, 77–78	438.37	32	9.000E–05	5.830E–04	221.20	138.65	0.154	1.595	7	Recrystallized sandstone

Lithologic units are from **Harris et al.** (2013b), **Harris et al.** (2013c), **Harris et al.** (2013e), and **Harris et al.** (2013f).

Table T4. Natural remanent magnetization of basalts, Sites U1381 and U1414.

Core, section, interval (cm)	Depth (mbsf)	Mass (g)	Volume (cm³)	Magnetic susceptibility (cm³/g)	Intensity (A/m)	Inclination (°)	Declination (°)	MAD (°)	Igneous unit
334-U1381A-									
14R-2, 41–42	110.39	4.426	1.58	102	4.50E+0	22.4	356.0	0.85	III
19R-1, 65–66	133.05	5.336	1.86	142	6.24E–1	20.0	186.0	6.41	III
24R-1, 52–53	154.02	3.685	1.30	118	6.08E–1	18.2	328.6	4.02	III
344-U1414A-									
46R-2, 87–88	378.41	3.665	1.27	112	3.78E–1	30.4	315.7	5.61	1
50R-2, 9–10	400.29	2.875	1.04	227	4.67E+0	7.60	232.5	1.11	3
54R-1, 120–121	419.40	4.584	1.59	330	2.65E–1	25.0	32.4	11.1	5
58R-3, 40–41	440.69	3.595	1.26	407	1.14E+1	–27.3	203.8	5.05	8
60R-1, 53–54	447.83	3.594	1.33	320	2.11E+0	0.4	328.4	2.05	8
62R-4, 50–51	461.59	3.905	1.39	324	1.66E+0	45.5	266.2	14.6	8

MAD = maximum angular deviation. Igneous units are from **Harris et al.** (2013c) and Expedition 334 Scientists (2012b).